CHEMISTRY OF MATERIALS

Open Access

pubs.acs.org/cm

Article

Ordered Cationic Mixing in a 1D Organic–Inorganic Hybrid

Published as part of Chemistry of Materials special issue "C. N. R. Rao at 90".

Megan A. Cassingham,[#] Sujeewa N. S. Lamahewage,[#] Yang G. Goh,[#] Alexander G. Squires, Aamani Ponnekanti, Sarah Karabadjakyan, Anna Wapner, Peter I. Djurovich, David O. Scanlon, Aaron J. Rossini, Mark E. Thompson, and Brent C. Melot*

Cite This: *Chem. Mater.* 2025, 37, 2418–2426

Read Online

ACCESS | Metrics & More | Article Recommendations | Supporting Information

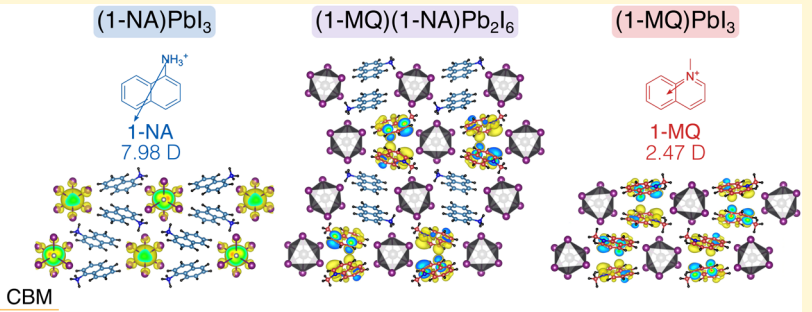

ABSTRACT: Hybrid metal halides are a remarkably dynamic family of materials that offer a flexible platform for exploring the novel crystal chemistry that emerges at the intersection of organic and inorganic solids. Herein, we report the discovery of a hybrid that contains two molecules effectively adopting isostructural geometry, (1-NA)PbI_3 and (1-MQ)PbI_3, and our attempts to create solid solutions of the two beyond the 1:1 ratio. Single-crystal X-ray diffraction, combined with solid-state NMR measurements, clearly show that despite having nearly identical steric geometry, the only mixed phase attained was the composition (1-MQ)(1-NA)Pb_2I_6, which exhibits a high degree of order between the two molecules. We propose that this ordering is primarily driven by local molecular dipoles, which ultimately creates a band structure in the blended phase that is highly characteristic of the end members, with little sign of rehybridization between the organic or inorganic components.

INTRODUCTION

Hybrid materials containing organic molecules packed alongside periodic arrays of metal halide polyhedra are ideal models for studying optoelectronic properties of solids.[1,2] The photophysics of hybrids with 1D topologies has been studied extensively because of the ease with which self-trapped excitons can be created.[3−5] While the impact of varying the halide and metal centers is commonly explored, very few reports examine the effect of mixing molecular cations within hybrid lattices. Instead, most studies examining phases with more than one organic moiety in three-[6−9] and two-dimensional structures[10−18] more frequently feature distinct crystallographic positions where the two organics segregate.

Here, we report the structure of a one-dimensional hybrid, (1-MQ)(1-NA)Pb_2I_6, that contains two similarly shaped organic cations, 1-methylquinolinium (1-MQ) and 1-naphthylammonium (1-NA), representing a pseudo solid solution of the two end members, (1-NA)PbI_3 and (1-MQ)PbI_3. The nuclear structure of the mixed system was characterized using a combination of single-crystal X-ray diffraction and solid-state NMR techniques in order to discriminate the near-identical compositions of the molecular constituents. In addition to the (1-MQ)(1-NA)Pb_2I_6 system, the end-member hybrids, (1-NA)PbI_3 and (1-MQ)PbI_3, were characterized and provide insight into the packing of the discrete organic components. We find that clear differences in the electronic structure between the 1-MQ and 1-NA cations drive the minor variation between structures and the differences seen between the octahedra in (1-MQ)(1-NA)Pb_2I_6. These results reinforce the notion that spatial proximity between two molecules is insufficient to achieve admixing of their electronic orbitals, which can remain a significant challenge for achieving efficient charge transfer through these hybrid materials.

Received: August 22, 2024
Revised: March 3, 2025
Accepted: March 4, 2025
Published: March 25, 2025

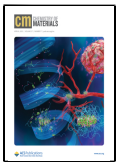

EXPERIMENTAL DETAILS

The precursor salt, 1-methylquinolinium iodide ($C_{10}H_{10}NI$, (1-MQ)I), was synthesized by mixing 2 parts quinoline (98%, Sigma-Aldrich) with iodomethane (99%, stable with Cu, Fisher) in approximately 10 mL of acetonitrile (HPLC, EMD Millipore). The solution was then heated to 85 °C and stirred for 2 h. Once the solution cooled to room temperature, it was transferred to a glass Petri dish to allow the solvent to evaporate. The resulting yellow solid was vacuum-filtered and rinsed with diethyl ether (≥98% (stabilized), VWR). Proton NMR spectra using DMSO-d_6 (Cambridge Isotope Laboratories) were collected to confirm the purity and structure of the product (reported in the Supporting Information).

1-Methylquinolinium lead iodide ((1-MQ)PbI_3) was prepared by dissolving 0.2 g (0.43 mmol) of lead(II) iodide (PbI_2, 99.9985% (metals basis), Alfa Aesar) and 0.12 g (0.44 mmol) of the prepared (1-MQ)I salt in 2 and 3 mL of hydroiodic acid (HI, 57 wt % (stabilized), Sigma-Aldrich) in 2 dram and 8 dram scintillation vials, respectively. The organic salt solution was stirred continuously in an aluminum bead bath on a hot plate until reaching 100 °C. Once all solids were dissolved in both solutions, the lead solution was decanted into the organic solution and allowed to briefly mix before the heat. The resulting yellow crystals were collected via vacuum filtration and rinsed with acetone (≥99.5%, VWR).

1-Naphthylammonium lead iodide ((1-NA)PbI_3) was prepared following the same procedure using 0.2 g of PbI_2 (0.43 mmol) and 0.078 g (0.54 mmol) of 1-naphthylamine ($C_{10}H_9N$, 99%, Sigma-Aldrich). The resulting product was vacuum-filtered and rinsed with diethyl ether.

The mixed hybrid (1-MQ)(1-NA)Pb_2I_6 was synthesized by using the same procedure. The lead solution was made by dissolving 0.2 g (0.43 mmol) of PbI_2 with 2 mL HI in a 2 dram vial. The organic salt solution was made by dissolving 0.038 g (0.27 mmol) of 1-naphthylamine and 0.056 g (0.21 mmol) (1-MQ)I with 5 mL of HI in an 8 dram vial. The resulting product was vacuum-filtered and rinsed with diethyl ether. (1-NA)PbI_3 and (1-MQ)(1-NA)Pb_2I_6 were both stored in an Ar glovebox to avoid degradation due to atmospheric exposure.

1-Naphthylamine-d_3 chloride salt was synthesized to create a deuterated version of the mixed hybrid for solid-state NMR experiments. 100 mg of 1-naphthylamine was heated and dissolved in 10 mL of deuterium chloride (DCl, 20% w/w in D_2O, 99.5% isotopic). The resulting product was analyzed by NMR and used to synthesize the mixed hybrid. (1-MQ)(1-NA-d_3)Pb_2I_6 was synthesized by using the same procedure outlined above with the expectation that some back conversion of the deuterons to protons would occur. Any resulting back conversion did not affect the solid-state NMR experiments significantly.

Single-crystal data for (1-MQ)PbI_3 and (1-MQ)(1-NA)Pb_2I_6 were collected at 100 K by using a Rigaku XTALab Synergy diffractometer with a CCD area detector. The data reduction was performed using Crysalis Pro and refined using Olex2 with the ShelXL program installed.[19] Single-crystal data was also collected for (1-NA)PbI_3 to confirm the structure first reported by Lemmerer and Billing and later reported with minor lattice changes by Mitrofanov et al.[20,21]

Solid-state NMR spectroscopy experiments were performed on a 9.4 T Bruker wide-bore magnet equipped with a Bruker AVANCE III HD console (^{1}H spin echo, ^{207}Pb spin echo, ^{1}H{^{14}N} D-HMQC, ^{2}H spin echo, and ^{1}H{^{2}H} DE-RESPDOR) and equipped with a Bruker 1.3 mm HX probe with MAS frequency. All experiments utilized N_2 gas for spinning. ^{1}H chemical shifts were referenced to neat tetramethylsilane using adamantane (δ_{iso}(^{1}H) = 1.72 ppm) as a secondary chemical shift reference. ^{207}Pb and ^{2}H chemical shifts were indirectly referenced to neat TMS using the IUPAC recommended relative NMR frequency.[22] NMR spectra were processed and analyzed with Bruker TopSpin version 3.6.4 (AVANCE III HD data) software.

The following experimental details are with respect to data acquired at B_0 = 9.4 T with the 1.3 mm HX NMR probe. ^{1}H spin echo solid-state NMR spectra of (1-NA)PbI_3, (1-MQ)PbI_3, and (1-MQ)(1-NA)Pb_2I_6 were recorded with a 50 kHz MAS frequency, and the ^{1}H longitudinal relaxation time constants (T_1) were ca. 3.3, 19.3, and 6.9 s, respectively. All experiments utilized a 1.3 × T_1 s recycle delay. ^{207}Pb spin echo solid-state NMR spectra of (1-NA)PbI_3, (1-MQ)PbI_3, and (1-MQ)(1-NA)Pb_2I_6 were recorded with a 50 kHz MAS frequency, and all experiments utilized a 0.5 s optimized recycle delay. The ^{207}Pb isotropic chemical shift tensor parameter (δ_{iso}) was determined with the solid line shape analysis (SOLA) module in Bruker TopSpin 3.6.4 software.

For the ^{1}H{^{14}N} D-HMQC[2] solid-state NMR experiment, the symmetry-based $SR4_1^2$ dipolar recoupling sequence[23] was applied on the ^{1}H channel at the second-order rotary resonance recoupling condition.[24−26] The optimum total dipolar recoupling time used for (1-MQ)(1-NA)Pb_2I_6 was 1.28 ms, and the ^{14}N excitation and reconversion pulse lengths had a duration of one rotor period. The ^{14}N RF field was 62.1 kHz. ^{2}H spin echo solid-state NMR spectra of (1-MQ)(1-NA-d_3)Pb_2I_6 were recorded with a 20 kHz MAS frequency, and all experiments utilized a 0.1 s recycle delay. ^{1}H{^{2}H} DE-RESPDOR[9] experiments of (1-MQ)(1-NA-d_3)Pb_2I_6 were performed with 50 kHz MAS and ^{2}H saturation pulses that were 30 μs (1.5 × τ_{rot}) in duration with 107.5 kHz RF field. The $SR4_1^2$ heteronuclear dipolar recoupling sequence was applied to the ^{1}H spins to reintroduce the ^{1}H−^{2}H dipolar interaction under MAS.[23] A control (without a ^{2}H saturation pulse) and dephased (with a ^{2}H saturation pulse) point were recorded at each recoupling time considered in this experiment. The ^{1}H T_1 of (1-MQ)(1-NA-d_3)Pb_2I_6 was *ca.* 6.8 and 7.1 s for high-frequency (aromatic protons) and low-frequency (−CH_3) signals, respectively; all experiments utilized a 9.23 s recycle delay and considered the low-frequency signal (−CH_3) to construct the RESPDOR dephasing curve. The ^{2}H isotropic chemical shift (δ_{iso}), C_Q, and η were determined by extracting sideband manifolds from the one-dimensional (1D) spin echo spectrum and fitting the manifold with the SOLA module in the Bruker TopSpin 3.6.4 software. A summary of all experimental data is shown in Table S3.

SIMPSON v4.1.1 was used to run numerical solid-state NMR simulations.[27−29] The archived data include the SIMPSON input codes. Except for the ^{1}H $\pi/2$ pulses, all of the pulses in the files were finite in duration. The ^{1}H{^{2}H} DE-RESPDOR dephasing curves were simulated using the rep678 crystal file, 13 γ-angles, and 107.5 kHz ^{2}H RF field. The ^{1}H{^{2}H} DE-RESPDOR numerical simulations for the (1-MQ)(1-NA-d_3)Pb_2I_6 were done considering a multispin ^{1}H−^{2}H$_n$ (n = 3) system and corresponding Euler angles.

Density functional theory (DFT) calculations were performed using the projector-augmented wave method within the Vienna Ab Initio Simulation Package (VASP).[30,31] The density of states and band diagram plots were plotted using sumo.[32] Due to the size of the unit cells, the functional of Perdew, Burke, and Ernzerhof[33] was used for geometrical relaxation, while the functional of Heyd, Scuseria, and Ernzerhof (HSE06),[34,35] with the explicit inclusion of spin−orbit coupling (HSE06 + SOC), was used for electronic structure calculations, including density of states and electronic band structure, performed using the structures relaxed with PBEsol. A plane-wave kinetic energy cutoff of 600 eV and a 2 × 1 × 1 Γ-centered k-point grid was used such that total energy had converged to within 1 meV/atom. Geometry optimization was considered to have converged when the forces on each atom fell below 0.01 eV Å^{-1}, and the plane-wave cutoff was increased to 600 eV during relaxation to avoid Pulay stress. Partial charge density information was generated using pymatgen.[36]

Diffuse reflectance data was collected from 800 to 250 nm using a PerkinElmer Lambda 950 UV−vis−NIR spectrophotometer equipped with a 150 mm integrating sphere to determine the onset of absorption in powders diluted to 3 wt % in magnesium(II) oxide (MgO, 98%, ACROS Organics) and to approximate the optical band gap using the Kubelka−Munk transform.[37]

Temperature-dependent photoluminescence and lifetime data were collected from 3 to 290 K using neat solid samples. Each sample was sandwiched between two 1 mm thick sapphire disks before being placed in the cryostat system. Samples were excited at 365 nm, and data was collected from 400 to 800 nm for the steady state emission

https://doi.org/10.1021/acs.chemmater.4c02364
Chem. Mater. 2025, 37, 2418−2426

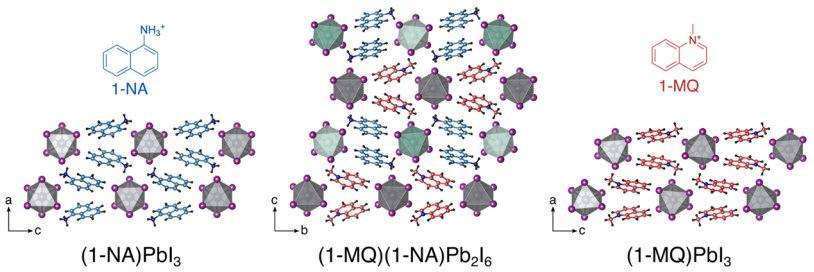

Figure 1. Crystal structures of $(1\text{-NA})PbI_3$, $(1\text{-MQ})(1\text{-NA})Pb_2I_6$, and $(1\text{-MQ})PbI_3$. 1-NA and 1-MQ cations are colored blue and red, respectively.

spectra using a Photon Technology International QuantaMaster model C-60SE spectrofluorimeter in tandem with a Janis model SHI-4-2 optical He cryostat equipped with a Lakeshore model 335 temperature controller.

RESULTS AND DISCUSSION

The synthesis of each phase yielded small yellow tabular crystallites. All three compositions adopt the *Pbca* space group, as shown in Figure 1, with the results from the refinement of the $(1\text{-MQ})PbI_3$ and $(1\text{-MQ})(1\text{-NA})Pb_2I_6$ structures presented in Tables S7 and S8. The inorganic portion of each 1-D material consists of similar face-sharing lead iodide octahedra. In $(1\text{-MQ})PbI_3$ and $(1\text{-NA})PbI_3$, the inorganic chains are parallel to the *b*-axis, while in $(1\text{-MQ})(1\text{-NA})Pb_2I_6$, the chains are parallel to the *a*-axis. Each of the end-member hybrids has one unique lead site, whereas the model for the mixed hybrid contains three distinct environments. Powder XRD was performed on all three hybrids to assess the phase purity of each material. Pawley fittings of the powder XRD patterns for $(1\text{-NA})PbI_3$, $(1\text{-MQ})PbI_3$, and $(1\text{-MQ})(1\text{-NA})Pb_2I_6$ (Figure S9) indicate that the bulk products are pure single-phase materials.

When comparing the end members, there are few differences in the structural topology aside from the identity of the organic cation. A small distortion to the intraoctahedral bond angles in $(1\text{-MQ})PbI_3$ can be seen because of the difference in location of the cationic charge center compared to $(1\text{-NA})PbI_3$. In $(1\text{-NA})PbI_3$, the inorganic octahedra have highly symmetrical bond lengths and angles. In $(1\text{-MQ})PbI_3$, the angles in the octahedra are distorted farther away from 90 and 180° to bring the iodine atoms closer to the nitrogen atoms in the quinolinium rings. This translates to a shorter distance of 4.09 Å between the quinolinium nitrogen and the iodine atoms in $(1\text{-MQ})PbI_3$ when compared to the 4.23 Å distance between the equivalent carbon atom in 1-NA and the iodine atoms of $(1\text{-NA})PbI_3$.

Hydrogen bonding appears to play a significant role in $(1\text{-NA})PbI_3$, whereas other electrostatic interactions are the driving force in $(1\text{-MQ})PbI_3$. The shortest ammonium nitrogen to iodine distance in $(1\text{-NA})PbI_3$ is 3.53 Å, which is on the longer end of the scale for hydrogen bonds. The shortest distance between a quinolinium nitrogen and iodine in $(1\text{-MQ})PbI_3$ is 4.09 Å, which is on the scale of other electrostatic interactions. Therefore, although hydrogen bonding is not possible in $(1\text{-MQ})PbI_3$, it does play a role in the cationic packing of 1-NA in $(1\text{-NA})PbI_3$.

Refinement of the single-crystal data for the mixed hybrid revealed a doubling of the *c*-axis relative to the *a*-axis in $(1\text{-NA})PbI_3$ and $(1\text{-MQ})PbI_3$, resulting in an approximate unit cell volume doubling. Since the carbon and nitrogen atoms in the 1-MQ and 1-NA cations are indistinguishable by X-ray methods, the atomic positions of those atoms could not be differentiated during the refinement. Despite not being able to definitively assign the carbon and nitrogen atom positions, the X-ray data indicate that the mixed hybrid does incorporate both cations and is not a solid solution, as seen in Figure 1.

Additionally, the lead iodide octahedra are either canted (green) or slightly distorted (gray) from fully symmetric depending on the lead site, reflecting the creation of two distinct metal environments in $(1\text{-MQ})(1\text{-NA})Pb_2I_6$ (Figure 1). The green octahedra tilt slightly in $(00l)$ planes, where the cations appear to be pointing in opposite directions in relation to the methyl or ammonium groups. In the $(00l)$ planes where the cations are facing more in the same direction, the gray octahedra instead distort to bring the iodide atoms closer to the nitrogen atoms. The cations pack in a more symmetrical way around the canted octahedra, leading to the whole unit shifting rather than distorting as it does at the gray lead site where the cations do not pack symmetrically around the octahedra.

Looking at the cationic packing around the octrahedral rods, the canted octahedra are surrounded by four 1-NA cations and two 1-MQ cations and vice versa for the distorted cations. Since the 1-NA cations exhibit hydrogen bonding interactions with the iodine atoms, they are more polarizable than the 1-MQ cations. Additionally, the dipole strengths of 1-NA and 1-MQ are 7.98 and 2.47 D, respectively. Consequently, it is reasonable to infer that the gray octahedra, which are surrounded by a greater number of the more rigid 1-MQ cations, would exhibit more significant distortion. In contrast, the green octahedra, surrounded by the softer and more polarizable 1-NA cations, exhibit canting rather than distortion.

To confirm the ordering between the 1-NA and 1-MQ cations in the crystal structure of $(1\text{-MQ})(1\text{-NA})Pb_2I_6$, we performed a variety of solid-state NMR experiments. Figure 2a–c shows ^1H spin echo solid-state NMR spectra of $(1\text{-NA})PbI_3$, $(1\text{-MQ})PbI_3$, and $(1\text{-MQ})(1\text{-NA})Pb_2I_6$. ^1H longitudinal relaxation time constants (T_1) were measured with saturation recovery experiments and gave values of ca. 3.3, 19.3, and 6.9 s for $(1\text{-NA})PbI_3$, $(1\text{-MQ})PbI_3$, and $(1\text{-MQ})(1\text{-NA})Pb_2I_6$, respectively. The observation of an intermediate ^1H T_1 for $(1\text{-MQ})(1\text{-NA})Pb_2I_6$ is consistent with the mixing of cations in the same crystalline lattice. The ^1H solid-state NMR spectra of all compounds show two main sets of ^1H NMR signals, with the lower-frequency signals having maximum intensity around 5.5 ppm, and the second higher-frequency signals having maximum intensity around 8.5 ppm. For $(1\text{-MQ})PbI_3$ and $(1\text{-MQ})(1\text{-NA})Pb_2I_6$, the low-frequency ^1H NMR signal is assigned to methyl groups of 1-MQ. For all compounds, the high-frequency ^1H NMR signals primarily arise from aromatic hydrogen atoms.

https://doi.org/10.1021/acs.chemmater.4c02364
Chem. Mater. 2025, 37, 2418−2426

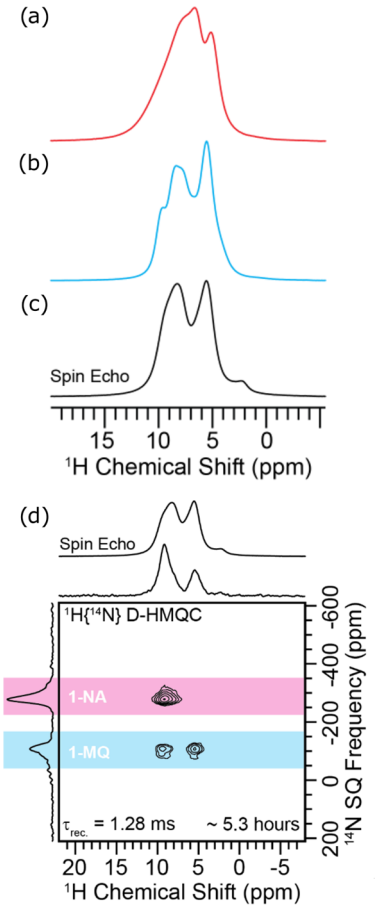

Figure 2. ^{1}H spin echo solid-state NMR spectra of (a) (1-NA)PbI_3, (b) (1-MQ)PbI_3, and (c) (1-MQ)(1-NA)Pb_2I_6. (d) ^{1}H{^{14}N} dipolar heteronuclear multiple quantum correlation (D-HMQC)[38] solid-state NMR spectrum of (1-MQ)(1-NA)Pb_2I_6. All NMR spectra were acquired with a 9.4 T magnetic field and a 50 kHz magic angle spinning (MAS) frequency.

^{1}H{^{14}N} dipolar heteronuclear multiple quantum correlation (D-HMQC)[1] experiments were performed on all three compounds. The ^{1}H{^{14}N} D-HMQC spectra show that the ammonium hydrogen atoms of 1-NA resonate at ca. 9 ppm, while the methyl protons of 1-MQ (which are adjacent to the quinoline nitrogen atom) resonate at 5.5 ppm (Figures 2d and S1). As expected, the indirect ^{14}N dimension clearly shows two distinct ^{14}N NMR signals. These NMR signals are centered at −280 and −107 ppm and are assigned the ammonium nitrogen of 1-NA and the quinolinium nitrogen of 1-MQ, respectively. These assignments are obvious when comparing the ^{1}H{^{14}N} D-HMQC spectra of each compound and considering the observed ^{1}H correlations (Figure S1). Both ^{14}N NMR signals have a single well-defined discontinuity, consistent with the presence of only one of each nitrogen atom in the asymmetric unit of the crystal structure of (1-MQ)(1-NA)Pb_2I_6.

Figure 3a–c shows ^{207}Pb solid-state NMR spectra of (1-NA)PbI_3, (1-MQ)PbI_3, and (1-MQ)(1-NA)Pb_2I_6, respectively. Peak fitting was used to determine the isotropic chemical shifts (δ_{iso}) of each ^{207}Pb solid-state NMR spectra shown in Figure 3. The δ_{iso} for ^{207}Pb solid-state NMR spectra of each (1-NA)PbI_3 and (1-MQ)PbI_3 hybrid systems are 952 and 891 ppm, respectively. The mixed-cation (1-MQ)(1-NA)Pb_2I_6 shows a ^{207}Pb spectrum with a peak that is similar in breadth to that of

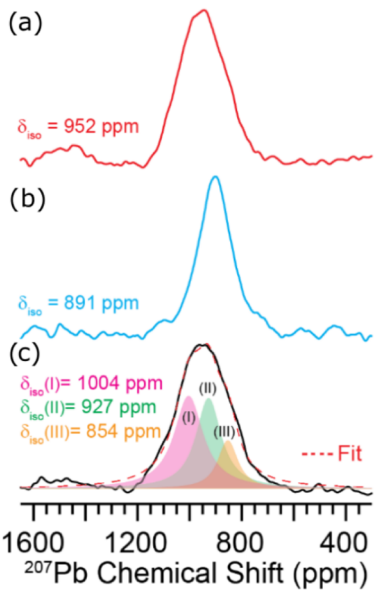

Figure 3. ^{207}Pb spin echo solid-state NMR spectra of (a) (1-NA)PbI_3, (b) (1-MQ)PbI_3, and (c) (1-MQ)(1-NA)Pb_2I_6. All NMR spectra were acquired with a 9.4 T magnetic field and a 50 kHz magic angle spinning (MAS) frequency.

(1-NA)PbI_3, which is somewhat surprising given that there are three distinct Pb atoms in the asymmetric unit of the crystal structure of (1-MQ)(1-NA)Pb_2I_6. However, it is well known that lead and tin iodide perovskites often give rise to homogeneously broadened ^{119}Sn and ^{207}Pb NMR signals.[39−43] The homogeneous broadening arises from the strong scalar and dipolar couplings between ^{207}Pb and ^{127}I (a 100% abundant I = 5/2 nucleus) and dynamic exchange of iodide atoms or fast ^{127}I relaxation that is caused by sizable quadrupolar interactions.[41,42] Due to the homogeneous broadening of the ^{207}Pb solid-state NMR spectra, it is difficult to observe distinct ^{207}Pb NMR signals for (1-MQ)(1-NA)Pb_2I_6.

^{1}H{^{207}Pb} t_1-noise eliminated (TONE) D-HMQC[44] were performed on all three compounds (Figure S2). These experiments show correlations between the ^{207}Pb NMR signals and ^{1}H NMR signals of both cations, confirming that the cations are within 5 Å of the Pb atoms in all systems. Interestingly, extracting ^{207}Pb NMR spectra at different ^{1}H chemical shifts (columns) from the 2D ^{1}H{^{207}Pb} TONE D-HMQC spectrum of (1-MQ)(1-NA)Pb_2I_6 results in partial resolution of distinct ^{207}Pb NMR signals, consistent with the presence of multiple Pb sites in the asymmetric unit of this compound (Figure S2).

We also performed plane-wave density functional theory including projector-augmented wave (GIPAW)[45] calculations on all compounds. These calculations predict that ^{207}Pb isotropic chemical shielding (σ_{iso}) is 6906 and 6860 ppm for (1-NA)PbI_3 and (1-MQ)PbI_3 hybrid systems, respectively. In contrast, for the (1-MQ)(1-NA)Pb_2I_6, three different ^{207}Pb sites were predicted with σ_{iso} = 6604, 6796, and 6898 ppm (Figure 3c).

The ^{1}H → ^{13}C cross-polarization (CP) solid-state NMR spectra of (1-MQ)(1-NA)Pb_2I_6 provide additional evidence for ordering of the cation positions in (1-MQ)(1-NA)Pb_2I_6. ^{1}H → ^{13}C 2D CP-HETCOR NMR spectra are shown in Figure S4 and confirm ^{1}H NMR signal assignments. The ^{1}H →

https://doi.org/10.1021/acs.chemmater.4c02364
Chem. Mater. 2025, 37, 2418−2426

^{13}C CP solid-state NMR spectra show similar full widths at half-height (fwhh) of ca. 152 Hz and ca. 169 Hz for the methyl ^{13}C NMR signals of (1-MQ)PbI_3 and (1-MQ)(1-NA)Pb_2I_6, respectively (Figure S3). In the crystal structure of (1-MQ)PbI_3, all methyl groups reside at symmetry-related positions. Therefore, the observation of a similar fwhh for the methyl ^{13}C NMR signals of (1-MQ)PbI_3 and (1-MQ)(1-NA)Pb_2I_6 suggests that the methyl positions are also ordered in the latter. Consistent with this hypothesis, the experimental X-ray crystal structure of (1-MQ)(1-NA)Pb_2I_6 shows that 1-MQ and 1-NA are arranged in a regular manner. All 1-MQ methyl groups reside in the same symmetry-related position, and 1-MQ methyl groups always neighbor the 1-NA amine group (Figure S5). DFT GIPAW calculations predict that there is only a single calculated ^{13}C magnetic shielding value for the experimental crystal structure. Using DFT, we made an alternative model of the crystal structure where the positions of 1-NA and 1-MQ are disordered (Figure S5). In this model, there are now four distinct 1-MQ methyl groups. DFT GIPAW calculations predict that there is up to a 2.1 ppm difference in magnetic shielding for the different methyl groups (Table S1). Therefore, the calculations suggest that if there was disorder in the 1-MQ and 1-NA positions there would likely be sizable inhomogeneous broadening on the order of 2 ppm, or distinct ^{13}C NMR signals could be observed for different 1-MQ molecules within the lattice. Both of these predictions are inconsistent with the experimental ^{13}C solid-state NMR spectra, again suggesting there is ordering of the 1-MQ and 1- NA positions in the lattice.

Finally, we prepared a sample of (1-MQ)(1-NA)Pb_2I_6 where the hydrogen on the ammonium was replaced with deuterium to enable ^{2}H solid-state NMR experiments. As discussed below, the ^{2}H-labeling enabled us to perform ^{1}H−^{2}H dipolar coupling measurements that can probe the distance between methyl and ammonium protons of 1-MQ and 1-NA.

Figure 4a shows the ^{2}H spin echo solid-state NMR spectrum (black) acquired at B_0 = 9.4 T magnetic field with a 20 kHz MAS frequency, and the simulation is shown in cyan. The ^{2}H isotropic chemical shift (δ_{iso}), quadrupolar coupling constant (C_Q), and asymmetry parameter (η) were obtained by fitting the peak intensities of the sideband manifold. The simulation gives the ^{2}H δ_{iso}, C_Q, and η values, which are 7.1 ppm, 164 kHz, and 0.12, respectively. The measured C_Q values suggest that there is relatively slow reorientation of the ND_3 groups on the ^{2}H NMR time scale.

Figure 4b shows ^{1}H{^{2}H} DE-RESPDOR[23,46] dephased spectrum (red, S) recorded with ^{2}H saturation pulses and the control spectrum (black, S_0) recorded without saturation pulses. The difference spectrum (S_0-S, green) is illustrated below. A plot of $1 - S/S_0$ as a function of the recoupling duration yields the dephasing curve (Figure S7a). Here, all experimental data points correspond to the dephasing observed at the methyl protons of the 1-MQ; although due to the limited resolution of the ^{1}H NMR spectra, the dephasing from the aromatic ^{1}H spins will also contribute. With knowledge of ^{2}H, C_Q, and η, the ^{1}H{^{2}H} DE-RESPDOR dephasing curve for the deuterated (1-MQ)(1-NA)Pb_2I_6 can be modeled. Multispin ^{1}H−^{2}H (n = 3) numerical SIMPSON simulations were performed to model the dephasing curve. In order to simplify the analysis, we assume that the dipolar couplings are the same for all of the ^{1}H−^{2}H spin pairs. Although the crystal structure of (1-MQ)(1-NA)Pb_2I_6 suggests

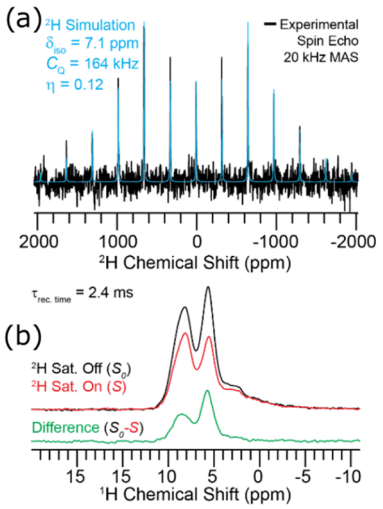

Figure 4. (a) ^{2}H spin echo solid-state NMR spectrum (black) of (1-MQ)(1-NA)Pb_2I_6 hybrid system in a 9.4 T magnetic field with a 20 kHz MAS frequency. The peak fitting is shown in a cyan solid line. (b) ^{1}H{^{2}H} DE-RESPDOR spectra recorded (red) with or (black) without 30 μs ^{2}H saturation pulses. The difference spectrum (green) is shown below. Both spectra were acquired in a 9.4 T magnetic field with a 50 kHz MAS frequency.

unique ^{1}H−^{2}H distances for each hydrogen and deuterium atom, it is important to keep in mind that the methyl groups are likely rotating with MHz frequencies, which will result in partial averaging of the dipolar coupling constants and a perceived increase in internuclear distances. A root-mean-square deviation (RMSD) calculation was utilized to identify the best-fit ^{1}H−^{2}H distance. This analysis suggested that the average ^{1}H−^{2}H distance is 3.8 Å between the methyl protons of 1-MQ and the ^{2}H of the 1-NA molecule (Figure S6).

Figure S7b shows part of the crystal structure of (1-MQ)(1-NA)Pb_2I_6, illustrating the distances between the methyl group of 1-MQ and the nearest ammonium groups of 1-NA. Note that plane-wave DFT was used to optimize the hydrogen atom positions in this structure. The distance for the methyl hydrogen (H atom q) to the three nearest ammonium hydrogen atoms (H atoms a, b, and c) is 3.95 Å. For all of the methyl protons, the average distance to the nearest three ammonium protons is 4.45 Å (Table S2). While our measured value of 3.8 Å is shorter than this average value, it is important to keep in mind that there are additional nearby ammonium groups in the lattice that will also contribute to the dephasing in the ^{1}H{^{2}H} RESPDOR experiments, explaining why the measured distance is shorter than the average distance seen in the DFT optimized crystal structure. In summary, the ^{1}H{^{2}H} RESPDOR experiments are consistent with the proposed crystal structure of (1-MQ)(1-NA)Pb_2I_6 that shows ordering of the 1-NA and 1-MQ positions in the lattice that results in the hydrogen atoms of the methyl and ammonium groups being separated by 4.45 Å on average.

Solid-state NMR spectroscopy confirmed that the 1-NA and 1-MQ cations are indeed packed within the same crystal structure and are ordered. However, this method does not confirm the specific positions of the 1-NA and 1-MQ cations. In order to rationalize the final packing configuration shown in Figure 1, we projected the dipole moments of 1-NA and 1-MQ onto the structures, as shown in Figure S8. The dipole strengths of 1-NA and 1-MQ are 7.98 and 2.47 D, respectively.

https://doi.org/10.1021/acs.chemmater.4c02364
Chem. Mater. 2025, 37, 2418−2426

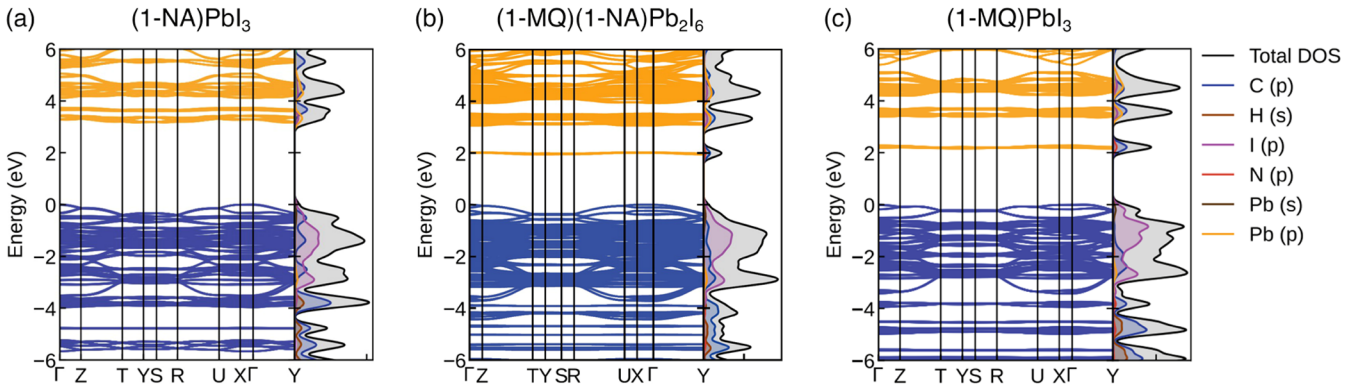

Figure 5. Combined DOS and band structure plots for (a) (1-NA)PbI_3, (b) (1-MQ)(1-NA)Pb_2I_6, and (c) (1-MQ)PbI_3.

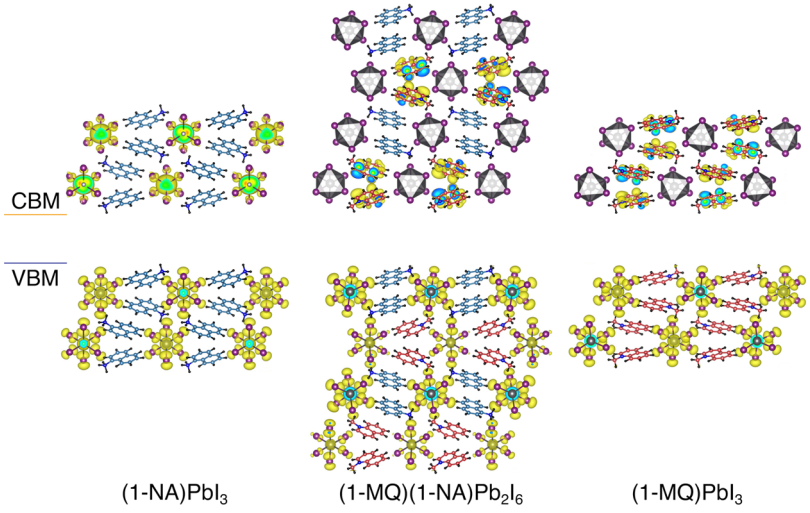

Figure 6. Charge density at the conduction band minimum and valence band maximum of (1-NA)PbI_3, (1-MQ)(1-NA)Pb_2I_6, and (1-MQ)PbI_3.

Due to the significantly larger dipole moment of 1-NA, it is reasonable to assign 1-NA to cationic positions where their dipoles would cancel out in short proximity. In contrast, the 1-MQ cations, with weaker dipole moments, are assigned to positions where there is a net dipole moment within the (00*l*) planes.

The octahedral distortion in (1-MQ)(1-NA)Pb_2I_6 is also nicely contrasted to that of the octahedral distortion in (1-MQ)PbI_3. As illustrated in Figure S8, there is a stronger net dipole moment within the (00*l*) plane in (1-MQ)PbI_3, resulting in a larger octahedral distortion compared to (1-MQ)(1-NA)Pb_2I_6. As for (1-NA)PbI_3, we can observe that the dipole moments of 1-NA cations are canceled out immediately with its neighboring cations. The tendency of 1-NA cations to have dipole cancellation in close proximity compared to 1-MQ cations, as illustrated with the end-member hybrids (1-MQ)PbI_3 and (1-NA)PbI_3, further supports our designation of the 1-MQ and 1-NA cations in (1-MQ)(1-NA)Pb_2I_6.

Based on the density of states and band diagram data, it is evident that (1-MQ)(1-NA)Pb_2I_6 and (1-MQ)PbI_3 have similar conduction band characters as seen in Figure 5b,c. Each material displays an isolated band with cationic character, which contrasts the continuous nature seen in the bands of (1-NA)PbI_3 in Figure 5a. These isolated bands represent the lower LUMO energy of the 1-MQ cation in relation to the 1-NA cation. Additionally, the bands in all three systems are quite flat and do not display much dispersivity. Each system is also an indirect band gap semiconductor.

Charge density projections visualized using VESTA also reveal interesting differences between the materials. Figure 6 shows the projected charge densities for (1-MQ)PbI_3 and (1-NA)PbI_3 at the conduction band minimum (CBM) and valence band maximum (VBM) of each system. In the case of (1-NA)PbI_3, the charge density is localized around the inorganic portion of the system at the band edges. Probing further into each band reveals some differences in the charge density map, but the localization stays around the inorganic octahedra. In (1-MQ)PbI_3, the charge density shifts from the inorganic octahedra at the VBM to the π-orbitals of the 1-MQ cations at the CBM. The charge density largely remains localized around the inorganic octahedra and organic cations in the valence and conduction bands, respectively. (1-MQ)(1-NA)Pb_2I_6 displays electronic properties very similar to (1-MQ)PbI_3. Figure 6 shows the charge densities at the VBM and CBM for (1-MQ)(1-NA)Pb_2I_6. The VBM displays inorganic character around all octahedra and the CBM displays organic character localized around the 1-MQ cations. Going deeper into the conduction band reveals further organic character. Deeper in the valence band, differing charge density around the inorganic octahedra is observed. While the charge density does not point to any interesting charge transfer phenomenon, it does demonstrate the connection between the (1-MQ)PbI_3 and (1-MQ)(1-NA)Pb_2I_6 systems.

https://doi.org/10.1021/acs.chemmater.4c02364
Chem. Mater. 2025, 37, 2418−2426

When compared to the experimental data, the computational data show similar trends in band gap values. While the computational and experimental values do not match exactly, (1-MQ)(1-NA)Pb_2I_6 has the smallest band gap and (1-NA)PbI_3 has the largest band gap with the (1-MQ)PbI_3 band gap falling between the two but closer to (1-MQ)(1-NA)Pb_2I_6. The experimental diffuse reflectance data shown as normalized Kubelka–Munk transforms can be seen in Figure S10.

The different electronic behaviors of (1-NA)PbI_3, (1-MQ)(1-NA)Pb_2I_6, and (1-MQ)PbI_3 observed in the computational data are reflected in their temperature-dependent emission properties. For (1-NA)PbI_3 (Figure S11a), we observe an increase in emission intensity as the temperature decreases. Below 40 K, the broad emission peak begins to red-shift, accompanied by an emergence of a vibronic structured triplet emission from the 1-NA cation. This results in a final broad emission centered around 656 nm, and a more intense triplet emission at approximately 500 nm.

In contrast, the (1-MQ)PbI_3 system does not exhibit a triplet emission. Instead, it shows a broad emission centered around 620 nm with minor energy shifts across the temperature range studied, as illustrated in Figure S11c. Additionally, the emission intensity of (1-MQ)PbI_3 peaks at 60 K and decreases as the temperature continues to drop.

The temperature-dependent powder emission of (1-MQ)(1-NA)Pb_2I_6 reveals a unique combination of emission profiles observed in (1-NA)PbI_3 and (1-MQ)PbI_3. The 508 nm emission feature starts to emerge at 50 K and continues to increase in intensity as the temperature decreases. This is reminiscent of the triplet emission feature observed in (1-NA)PbI_3, albeit emerging at a lower temperature and not vibronic in nature. The more prominent broad emission feature is centered around 612 nm, and red-shifts to a wavelength of 625 nm at higher temperatures. Moreover, the emission intensity peaks at 5 K before decreasing at higher temperatures. The broad emission energy and temperature-dependent behavior resemble that of (1-MQ)PbI_3.

The difference in the emission properties of the two end-member hybrids is likely due to the differing LUMO energies of the two organic cation species. For (1-NA)PbI_3, the LUMO of 1-NA is higher than the CBM. At room temperature, while there is a possibility for electrons to excite to the triplet states, they quickly relax down to the CBM before radiatively decaying to the ground state. As the hybrid system cools, the pathways for nonradiative decay decrease due to the reduction of molecular and phonon vibrations, leading to an increase in emission intensity. At temperatures below 100 K, the energy needed to depopulate the triplet states decreases, resulting in the onset of triplet emission.

In the case of (1-MQ)PbI_3, the LUMO of 1-MQ is isolated and lower in energy than the rest of the conduction band. At room temperature, the electrons excite from the VBM into the LUMO of 1-MQ. As the (1-MQ)PbI_3 system cools, the reduction in molecular and phonon vibrations leads to an increase in emission intensity. At temperatures below 65 K, we hypothesize that the LUMO of 1-MQ acts as a trap state, reducing the radiative decay of the hybrid.

CONCLUSIONS

In summary, we have demonstrated, using a combination of single-crystal X-ray and solid-state NMR spectroscopy, that the molecular cations in (1-MQ)(1-NA)Pb_2I_6 prefer to pack in an ordered fashion. The large difference in the dipoles of the 1-NA and 1-MQ cations gives rise to minor differences in the lead sites and may contribute to the ability to overcome the entropy and avoid random packing. This material is the first of its kind, demonstrating the possibility to further explore this space and target stronger donor–acceptor pairs to create more interesting charge transfer characteristics.

ASSOCIATED CONTENT

Supporting Information

The Supporting Information is available free of charge at https://pubs.acs.org/doi/10.1021/acs.chemmater.4c02364.

^{1}H NMR of 1-methylquinolinium iodide (1-MQ)I salt, additional details of the crystallographic analysis, and solid-state NMR (PDF)

AUTHOR INFORMATION

Corresponding Author

Brent C. Melot − *Department of Chemistry, University of Southern California, Los Angeles, California 90089, United States; Mork Family Department of Chemical Engineering and Materials Science, University of Southern California, Los Angeles, California 90089, United States;* orcid.org/0000-0002-7078-8206; Email: melot@usc.edu

Authors

Megan A. Cassingham − *Department of Chemistry, University of Southern California, Los Angeles, California 90089, United States;* orcid.org/0000-0001-7702-5511

Sujeewa N. S. Lamahewage − *Ames National Laboratory, Division of Materials Science and Engineering, Ames, Iowa 50011, United States; Department of Chemistry, Iowa State University, Ames, Iowa 50011, United States;* orcid.org/0000-0002-8160-1056

Yang G. Goh − *Department of Chemistry, University of Southern California, Los Angeles, California 90089, United States;* orcid.org/0000-0003-1086-4876

Alexander G. Squires − *School of Chemistry, University of Birmingham, Birmingham B15 2TT, United Kingdom;* orcid.org/0000-0001-6967-3690

Aamani Ponnekanti − *Department of Chemistry, University of Southern California, Los Angeles, California 90089, United States; Mork Family Department of Chemical Engineering and Materials Science, University of Southern California, Los Angeles, California 90089, United States*

Sarah Karabadjakyan − *Department of Chemistry, University of Southern California, Los Angeles, California 90089, United States*

Anna Wapner − *Department of Chemistry, University of Southern California, Los Angeles, California 90089, United States; Mork Family Department of Chemical Engineering and Materials Science, University of Southern California, Los Angeles, California 90089, United States*

Peter I. Djurovich − *Department of Chemistry, University of Southern California, Los Angeles, California 90089, United States;* orcid.org/0000-0001-6716-389X

David O. Scanlon − *School of Chemistry, University of Birmingham, Birmingham B15 2TT, United Kingdom;* orcid.org/0000-0001-9174-8601

Aaron J. Rossini − *Ames National Laboratory, Division of Materials Science and Engineering, Ames, Iowa 50011, United States; Department of Chemistry, Iowa State*

University, Ames, Iowa 50011, United States; orcid.org/0000-0002-1679-9203

Mark E. Thompson − *Department of Chemistry, University of Southern California, Los Angeles, California 90089, United States; Mork Family Department of Chemical Engineering and Materials Science, University of Southern California, Los Angeles, California 90089, United States;* orcid.org/0000-0002-7764-4096

Complete contact information is available at: https://pubs.acs.org/10.1021/acs.chemmater.4c02364

Author Contributions

#M.A.C., S.N.S.L., and Y.G.G. contributed equally to this work.

Notes

The authors declare no competing financial interest.

■ ACKNOWLEDGMENTS

The authors acknowledge the NSF under DMR-1905826 for support of the synthesis and materials characterization work and CHE-2018740 for acquisition of supporting instrumentation. Solid-state NMR experiments and data analysis (S.N.S.L. and A.J.R.) were supported by the U.S. Department of Energy (DOE), Office of Science, Basic Energy Sciences, Materials Science and Engineering Division. The Ames Laboratory is operated for the U.S. DOE by Iowa State University under Contract DE-AC02-07CH11358. This work utilized Anvil at Purdue University through allocation MAT240024 from the Advanced Cyberinfrastructure Coordination Ecosystem: Services & Support (ACCESS) program, which is supported by National Science Foundation Grants #2138259, #2138286, #2138307, #2137603, and #2138296 for preliminary calculations. More intensive computational work utilized the University of Birmingham's BlueBEAR HPC service, the Baskerville Tier 2 HPC service (https://www.baskerville.ac.uk); funded by the EPSRC and UKRI through the World Class Laboratories scheme (EP/T022221/1) and the Digital Research Infrastructure programme (EP/W032244/1), and the Sulis Tier 2 HPC platform hosted by the Scientific Computing Research Technology Platform at the University of Warwick (funded by EPSRC Grant EP/T022108/1 and the HPC Midlands + consortium). Through our membership of the UK's HEC Materials Chemistry Consortium, which is funded by the UK Engineering and Physical Sciences Research Council (EPSRC; EP/L000202, EP/R029431, EP/T022213), this work also used ARCHER2 UK National Supercomputing Services. We are also grateful to the UK Materials and Molecular Modelling Hub for computational resources, which is partially funded by EPSRC (EP/T022213/1, EP/W032260/1, and EP/P020194/1).

■ REFERENCES

(1) Saparov, B.; Mitzi, D. B. Organic-Inorganic Perovskites: Structural Versatility for Functional Materials Design. *Chem. Rev.* **2016**, *116*, 4558−4596.

(2) Grancini, G.; Nazeeruddin, M. K. Dimensional tailoring of hybrid perovskites for photovoltaics. *Nat. Rev. Mater.* **2019**, *4*, 4−22.

(3) Yuan, Z.; Zhou, C.; Tian, Y.; Shu, Y.; Messier, J.; Wang, J. C.; Van De Burgt, L. J.; Kountouriotis, K.; Xin, Y.; Holt, E.; Schanze, K.; Clark, R.; Siegrist, T.; Ma, B. One-dimensional organic lead halide perovskites with efficient bluish white-light emission. *Nat. Commun.* **2017**, *8*, No. 14051.

(4) Wu, X.; Trinh, M. T.; Niesner, D.; Zhu, H.; Norman, Z.; Owen, J. S.; Yaffe, O.; Kudisch, B. J.; Zhu, X. Y. Trap states in lead iodide perovskites. *J. Am. Chem. Soc.* **2015**, *137*, 2089−2096.

(5) Ishida, K. Self-trapping dynamics of excitons on a one-dimensional lattice. *Z. Phys. B* **1997**, *102*, 483−491.

(6) Pellet, N.; Gao, P.; Gregori, G.; Yang, T. Y.; Nazeeruddin, M. K.; Maier, J.; Grätzel, M. Mixed-Organic-Cation Perovskite Photovoltaics for Enhanced Solar-Light Harvesting. *Angew. Chem., Int. Ed.* **2014**, *53*, 3151−3157.

(7) Saliba, M.; Matsui, T.; Seo, J. Y.; Domanski, K.; Correa-Baena, J. P.; Nazeeruddin, M. K.; Zakeeruddin, S. M.; Tress, W.; Abate, A.; Hagfeldt, A.; Grätzel, M. Cesium-Containing Triple Cation Perovskite Solar Cells: Improved Stability, Reproducibility and High Efficiency. *Energy Environ. Sci.* **2016**, *9*, 1989−1997.

(8) Zhao, Z.; Gu, F.; Li, Y.; Sun, W.; Ye, S.; Rao, H.; Liu, Z.; Bian, Z.; Huang, C. Mixed-Organic-Cation Tin Iodide for Lead-Free Perovskite Solar Cells with an Efficiency of 8.12%. *Adv. Sci.* **2017**, *4*, No. 1700204.

(9) Mateen, M.; Arain, Z.; Yang, Y.; Liu, X.; Ma, S.; Liu, C.; Ding, Y.; Ding, X.; Cai, M.; Dai, S. MACl-Induced Intermediate Engineering for High-Performance Mixed-Cation Perovskite Solar Cells. *ACS Appl. Mater. Interfaces* **2020**, *12*, 10535−10543.

(10) Mitzi, D. B.; Medeiros, D. R.; Malenfant, P. R. Intercalated organic-inorganic perovskites stabilized by fluoroaryl-aryl interactions. *Inorg. Chem.* **2002**, *41*, 2134−2145.

(11) Xu, Z.; Mitzi, D. B. SnI42−based hybrid perovskites templated by multiple organic cations: Combining organic functionalities through noncovalent interactions. *Chem. Mater.* **2003**, *15*, 3632−3637.

(12) Soe, C. M. M.; Stoumpos, C. C.; Kepenekian, M.; Traoré, B.; Tsai, H.; Nie, W.; Wang, B.; Katan, C.; Seshadri, R.; Mohite, A. D.; Even, J.; Marks, T. J.; Kanatzidis, M. G. New Type of 2D Perovskites with Alternating Cations in the Interlayer Space, (C(NH2)3)-(CH3NH3)nPbnI3n+1: Structure, Properties, and Photovoltaic Performance. *J. Am. Chem. Soc.* **2017**, *139*, 16297−16309.

(13) Lian, X.; Chen, J.; Qin, M.; Zhang, Y.; Lu, X.; Wu, G.; Chen, H.; Tian, S. The Second Spacer Cation Assisted Growth of a 2D Perovskite Film with Oriented Large Grain for Highly Efficient and Stable Solar Cells. *Angew. Chem., Int. Ed.* **2019**, *58*, 9409−9413.

(14) Xu, X.; Cao, K.; Zhu, W.; Gu, W.; Ma, B.; Qin, M.; Qian, J.; Lu, Y.; Liu, Z.; Chen, S.; Lu, X.; Huang, W. Improved Crystallization and Stability of Mixed-Cation Tin Iodide for Lead-Free Perovskite Solar Cells. *ACS Appl. Energy Mater.* **2020**, *3*, 5415−5426.

(15) Zhou, N.; Huang, B.; Sun, M.; Zhang, Y.; Li, L.; Lun, Y.; Wang, X.; Hong, J.; Chen, Q.; Zhou, H. The Spacer Cations Interplay for Efficient and Stable Layered 2D Perovskite Solar Cells. *Adv. Energy Mater.* **2020**, *10*, No. 1901566.

(16) Yan, L.; Jana, M. K.; Sercel, P. C.; Mitzi, D. B.; You, W. Alkyl-Aryl Cation Mixing in Chiral 2D Perovskites. *J. Am. Chem. Soc.* **2021**, *143*, 18114−18120.

(17) Wei, Q.; Ren, H.; Liu, J.; Liu, Q.; Wang, C.; Lau, T. W.; Zhou, L.; Bian, T.; Zhou, Y.; Wang, P.; Lei, Q.; Mohammed, O. F.; Li, M.; Yin, J. Long-Lived Hot Carriers in Two-Dimensional Perovskites: The Role of Alternating Cations in Interlayer Space. *ACS Energy Lett.* **2023**, *8*, 4315−4322.

(18) Zhuang, Q.; Li, H.; Zhang, C.; Gong, C.; Yang, H.; Chen, J.; Zang, Z. Synergistic Modification of 2D Perovskite with Alternating Cations in the Interlayer Space and Multisite Ligand toward High-Performance Inverted Solar Cells. *Adv. Mater.* **2023**, *35*, 2303275.

(19) Sheldrick, G. M. A short history of SHELX. *Acta Crystallogr., Sect. A* **2008**, *64*, 112−122.

(20) Lemmerer, A.; Billing, D. G. 1-Naphthylammonium triiodoplumbate(II). *Acta Crystallogr., Sect. E* **2006**, *62*, m904−m906.

(21) Mitrofanov, A.; Berencén, Y.; Sadrollahi, E.; Boldt, R.; Bodesheim, D.; Weiske, H.; Paulus, F.; Geck, J.; Cuniberti, G.; Kuc, A.; Voit, B. Molecular engineering of naphthalene spacers in low-dimensional perovskites. *J. Mater. Chem. C* **2023**, *11*, 5024−5031.

(22) Harris, R. K.; Becker, E. D.; Cabral de Menenzes, S. M.; Goodfellow, R.; Granger, P.*NMR Nomenclature. Nuclear Spin*

Properties and Conventions for Chemical Shifts (IUPAC Recommendations 2001), Proceedings of the 5th European Conference on Antennas and Propagation, 2001.
(23) Brinkmann, A.; Kentgens, A. P. Proton-selective 17O-1H distance measurements in fast magic-angle-spinning solid-state NMR spectroscopy for the determination of hydrogen bond lengths. *J. Am. Chem. Soc.* **2006**, *128*, 14758−14759.
(24) Oas, T. G.; Griffin, R. G.; Levitt, M. H. Rotary resonance recoupling of dipolar interactions in solid-state nuclear magnetic resonance spectroscopy. *J. Chem. Phys.* **1988**, *89*, 692−695.
(25) Hu, B.; Trébosc, J.; Amoureux, J. P. Comparison of several hetero-nuclear dipolar recoupling NMR methods to be used in MAS HMQC/HSQC. *J. Magn. Reson.* **2008**, *192*, 112−122.
(26) Cavadini, S.; Abraham, A.; Bodenhausen, G. Proton-detected nitrogen-14 NMR by recoupling of heteronuclear dipolar interactions using symmetry-based sequences. *Chem. Phys. Lett.* **2007**, *445*, 1−5.
(27) Tošner, Z.; Vosegaard, T.; Kehlet, C.; Khaneja, N.; Glaser, S. J.; Nielsen, N. C. Optimal control in NMR spectroscopy: Numerical implementation in SIMPSON. *J. Magn. Reson.* **2009**, *197*, 120−134.
(28) Bak, M.; Rasmussen, J. T.; Nielsen, N. C. SIMPSON: A General Simulation Program for Solid-State NMR Spectroscopy. *J. Magn. Reson.* **2000**, *147*, 296−330.
(29) Tošner, Z.; Andersen, R.; Stevensson, B.; Edén, M.; Nielsen, N. C.; Vosegaard, T. Computer-intensive simulation of solid-state NMR experiments using SIMPSON. *J. Magn. Reson.* **2014**, *246*, 79−93.
(30) Kresse, G.; Hafner, J. Ab initio molecular dynamics for liquid metals. *Phys. Rev. B* **1993**, *47*, 558.
(31) Kresse, G.; Hafner, J. Ab initio molecular-dynamics simulation of the liquid-metal−amorphous-semiconductor transition in germanium. *Phys. Rev. B* **1994**, *49*, No. 14251.
(32) Ganose, A. M.; Jackson, A. J.; Scanlon, D. O. sumo: Command-line tools for plotting and analysis of periodic *ab initio* calculations. *J. Open Source Software* **2018**, *3*, 717.
(33) Perdew, J. P.; Burke, K.; Ernzerhof, M. Generalized Gradient Approximation Made Simple. *Phys. Rev. Lett.* **1996**, *77*, 3865−3868.
(34) Heyd, J.; Scuseria, G. E.; Ernzerhof, M. Hybrid functionals based on a screened Coulomb potential. *J. Chem. Phys.* **2003**, *118*, 8207.
(35) Heyd, J.; Scuseria, G. E.; Ernzerhof, M. Hybrid functionals based on a screened Coulomb potential. *J. Chem. Phys.* **2003**, *118*, 8207−8215.
(36) Ong, S. P.; Richards, W. D.; Jain, A.; Hautier, G.; Kocher, M.; Cholia, S.; Gunter, D.; Chevrier, V. L.; Persson, K. A.; Ceder, G. Python Materials Genomics (pymatgen): A robust, open-source python library for materials analysis. *Comput. Mater. Sci.* **2013**, *68*, 314−319.
(37) Kubelka, P.; Munk, F. An Article on Optics of Paint Layers. *Z. Phys.* **1931**, *12*, 593−601.
(38) Mueller, L. Sensitivity Enhanced Detection of Weak Nuclei Using Heteronuclear Multiple Quantum Coherence. *J. Am. Chem. Soc.* **1979**, *101*, 4481−4484.
(39) Hanrahan, M. P.; Men, L.; Rosales, B. A.; Vela, J.; Rossini, A. J. Sensitivity-Enhanced 207Pb Solid-State NMR Spectroscopy for the Rapid, Non-Destructive Characterization of Organolead Halide Perovskites. *Chem. Mater.* **2018**, *30*, 7005−7015.
(40) Karmakar, A.; Askar, A. M.; Bernard, G. M.; Terskikh, V. V.; Ha, M.; Patel, S.; Shankar, K.; Michaelis, V. K. Mechanochemical Synthesis of Methylammonium Lead Mixed-Halide Perovskites: Unraveling the Solid-Solution Behavior Using Solid-State NMR. *Chem. Mater.* **2018**, *30*, 2309−2321.
(41) Kubicki, D. J.; Prochowicz, D.; Salager, E.; Rakhmatullin, A.; Grey, C. P.; Emsley, L.; Stranks, S. D. Local Structure and Dynamics in Methylammonium, Formamidinium, and Cesium Tin(II) Mixed-Halide Perovskites from 119Sn Solid-State NMR. *J. Am. Chem. Soc.* **2020**, *142*, 7813−7826.
(42) Shmyreva, A. A.; Safdari, M.; Furó, I.; Dvinskikh, S. V. NMR longitudinal relaxation enhancement in metal halides by heteronuclear polarization exchange during magic-angle spinning. *J. Chem. Phys.* **2016**, *144*, 224201.
(43) Rosales, B. A.; Men, L.; Cady, S. D.; Hanrahan, M. P.; Rossini, A. J.; Vela, J. Persistent Dopants and Phase Segregation in Organolead Mixed-Halide Perovskites. *Chem. Mater.* **2016**, *28*, 6848−6859.
(44) Venkatesh, A.; Luan, X.; Perras, F. A.; Hung, I.; Huang, W.; Rossini, A. J. T 1-Noise eliminated dipolar heteronuclear multiple-quantum coherence solid-state NMR spectroscopy. *Phys. Chem. Chem. Phys.* **2020**, *22*, 20815−20828.
(45) Pickard, C. J.; Mauri, F. All-electron magnetic response with pseudopotentials: NMR chemical shifts. *Phys. Rev. B* **2001**, *63*, 245101.
(46) Atterberry, B. A.; Carnahan, S. L.; Chen, Y.; Venkatesh, A.; Rossini, A. J. Double echo symmetry-based REDOR and RESPDOR pulse sequences for proton detected measurements of heteronuclear dipolar coupling constants. *J. Magn. Reson.* **2022**, *336*, No. 107147.

https://doi.org/10.1021/acs.chemmater.4c02364
Chem. Mater. 2025, 37, 2418−2426